LANGMUIR

pubs.acs.org/Langmuir Article

Investigations of the pH-Dependent Adsorption of Uranyl Species on Phosphorylated Cellulose-Nanocrystal Ferrihydrite: Insights from Combined Raman Spectroscopy and Computational Analyses

Tanmayaa Nayak, Sujan Manna, Ankita Narwal, Bijesh Kumar Malla, Sonali Seth, Sandeep K. Reddy, Sharma S. R. K. C. Yamijala,* and Thalappil Pradeep*

Cite This: *Langmuir* 2026, 42, 11219–11228 Read Online

ACCESS | Metrics & More | Article Recommendations | Supporting Information

ABSTRACT: Uranium contamination in groundwater is a major environmental concern due to its long half-life and chemical toxicity. We had previously developed the phosphorylated cellulose-nanocrystal–ferrihydrite (PCNCFH), a low-cost and sustainable nanomaterial, exhibiting a uranium adsorption capacity of 100 mg/g, and comprehensively characterized the adsorbent's performance and stability. In this study, we specifically focus on elucidating how environmentally relevant uranyl species such as $UO_2(CO_3)_3^{4-}$, $UO_2(CO_3)_2^{2-}$, and $(UO_2)_3(OH)_5^{+}$ interact with PCNCFH across the typical groundwater pH range of 5–9. Raman spectroscopy confirmed the speciation of uranyl complexes in solution, and time-dependent Raman measurements enabled us to quantify the adsorption kinetics and equilibrium adsorption capacities (q_e) of each species under controlled pH conditions. We find that $UO_2(CO_3)_3^{4-}$ exhibits significantly slower adsorption kinetics than the other complexes at all pH values. These results were also supported by IR spectroscopy and DFT modeling, revealing fundamental differences in interaction pathways that govern uranyl binding. Raman adsorption data were found to fit a pseudo-second-order model. The findings provide mechanistic insight essential for the rational design of species-specific and pH-optimized uranium remediation strategies for water utilities.

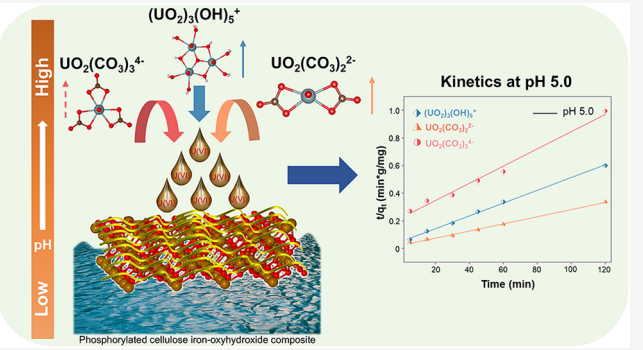

INTRODUCTION

Uranium is a significant contaminant in water due to its nephrotoxic effects on living organisms.[1] A survey conducted by the Ministry of Jal Shakti of India in 2020 revealed that 151 districts across 18 Indian states have groundwater with uranium concentrations exceeding 30 ppb, the threshold set by the WHO for safe drinking water.[2] Uranium contamination in groundwater arises from both anthropogenic sources (e.g., mining, nuclear power generation, and fertilizer use) and natural processes such as volcanic activity and rock weathering.[3] Naturally occurring uranium is a combination of three isotopes; ^{238}U, ^{235}U, and ^{234}U. Uranium can exhibit oxidation states ranging from +3 to +6, with +4 and +6 being the most prevalent in natural environments.[4] U(IV) predominates under mildly oxidizing to anoxic conditions and typically forms sparingly soluble hydrolysis products and microbially mediated oxide phases in natural waters, resulting in very low dissolved concentrations (0.01 μg/L).[5] Under aerobic conditions, U(VI) remains comparatively soluble in natural waters and occurs as the uranyl cation $[UO_2]^{2+}$, possessing strong covalent bonds with two axial oxygen atoms.[6,7] U(VI), classified as a hard Lewis acid, preferentially binds to oxygen, phosphorus,[8] and nitrogen-containing functional groups,[9] resulting in the formation of various soluble complexes and mineral phases in natural aquatic systems.[6] Accordingly, a wide range of adsorbents such as biosorbents,[10] zeolites,[11] carbon nanotubes,[12] activated carbon,[13] metal–organic frameworks (MOFs),[14] and metal oxides,[15] bearing these functional groups have demonstrated high efficiency in the remediation of U(VI). Among the various adsorbents, nanoscale metal oxides have been extensively applied for heavy metal remediation due to their excellent physicochemical stability under harsh conditions, such as elevated temperatures and highly acidic or alkaline pH environments.[16] Over the past decades, a wide range of metal oxide-based nanocomposites have been investigated for uranium removal, including TiO_2–CeO_2–Fe_2O_3 nanoparticles,[17] Fe_3O_4/rGO,[18] nano-rGO/TiO_2/CMC,[19] Fe_3O_4@SiO_2,[20] and magnetic Fe/Zn layered double

Received: January 16, 2026
Revised: March 29, 2026
Accepted: April 6, 2026
Published: April 11, 2026

oxide decorated carbon nanotubes (M-Fe/Zn-LDO@CNTs).[21]

In aquatic environments, uranium exists in multiple physicochemical species, such as the free ionic forms (U^{4+} or UO_2^{2+}), as well as coordination complexes with inorganic ligands like carbonate, nitrate, and sulfate, which coordinate directly within the inner coordination sphere.[22,23] Additionally, it can associate with natural organic matter, including humic and fulvic substances, and may be present in dissolved, colloidal, or particulate phases.[24,25] The chemical speciation of uranium is strongly influenced by environmental parameters such as ionic strength, pH, and solute concentration, which govern its coordination behavior and distribution among various aqueous phases.[26] In the binary UO_2^{2+}/H_2O system, at the pH range of 3−6, U(VI) favors the formation of cationic polynuclear uranyl hydroxo complexes, irrespective of ionic strength. Species such as trimers, dimers, and tetramers, e.g., $(UO_2)_3(OH)_5^+$, $(UO_2)_2(OH)_2^{2+}$, $(UO_2)_4(OH)_7^+$, $(UO_2)_4(OH)_6^{2+}$, and $(UO_2)_4(OH)_2^{6+}$ are thermodynamically stable in this pH regime. Among all these polynuclear hydroxo-uranyl species, $(UO_2)_3(OH)_5^+$ predominantly forms within the pH range of 5−6 under moderate total uranium concentrations (10^{-4}−10^{-3} M), irrespective of the ionic strength of the system. Within the pH range of 3−11, a closed ternary system of $UO_2^{2+}/CO_3^{2-}/H_2O$ facilitates the formation of predominant uranyl species such as $UO_2CO_3^{o}$, $(UO_2)_2CO_3(OH)_3^-$, $UO_2(CO_3)_2^{2-}$, and $UO_2(CO_3)_3^{4-}$ under conditions of 10^{-4} M uranium concentration, total carbon content between 400−600 mg/L, and ionic strength of 0.31 M. Formation of such uranyl carbonato complexes is strongly influenced by the concentration of bicarbonate ions present in the aqueous medium.[27,28]

Considering the complex speciation behavior of uranium in natural aquatic environments, a detailed understanding of its interaction with adsorbent surfaces is essential. Recent findings of uranium in human breast milk in several regions of Bihar,[29] India highlight the urgent need to understand uranium speciation under physiologically and environmentally relevant conditions. Identifying dominant uranyl species at physiological pH is essential for linking environmental exposure to potential maternal and infant uptake. Interactions with milk proteins, which provide oxygen- and nitrogen-donor sites, may further influence the uranyl transport and bioavailability. Uranium uptake by rice (a staple food in many regions) has also been investigated.[30] Because uranyl speciation governs its mobility, bioavailability, and toxicity, detailed speciation studies are essential for accurately assessing exposure risks and designing effective mitigation strategies. This necessitates the use of advanced analytical techniques capable of distinguishing between different uranyl species with high specificity and resolution. In this context, vibrational spectroscopy serves as a powerful and widely utilized analytical tool capable of differentiating various uranyl species by probing differences in their coordinating ligands, U−O bond strengths, and surrounding chemical environments.[31,32] Each uranyl complex exhibits unique vibrational modes, enabling its spectral identification. The symmetric (ν_1) and asymmetric (ν_3) stretching vibrations of the U−O of uranyl represent the most prominent modes observed in Raman and IR spectroscopy, respectively. Lu et al.[33] successfully established Raman spectroscopic methodology and identified U(VI) species at pH 3, 6, and 11 in the presence of carbonate. Their analysis revealed that U(VI) predominantly exists as UO_2^{2+} with a characteristic Raman band at 871 cm^{-1} at pH 3, as the fully coordinated carbonate complex $UO_2(CO_3)_3^{4-}$ with a feature at 814 cm^{-1} at pH 11, and as $UO_2(CO_3)_2^{2-}$ (836 cm^{-1}) and ($(UO_2)_2(OH)_2^{2+}$) (859 cm^{-1}) at pH 6 (basic and acidic solutions were prepared with Na_2CO_3 and HNO_3, respectively). Müller et al.[26] investigated U(VI) speciation in micromolar aqueous solutions by attenuated total reflection Fourier-transform infrared (ATR FT-IR) spectroscopy in conjunction with the updated the Nuclear Energy Agency Thermochemical Database (NEA TDB). They observed that under mildly acidic pH conditions, the trimer $(UO_2)_3(OH)_5^+$ is predicted to be a dominant species, exhibiting a characteristic IR absorption band at 923 cm^{-1}.[26] Liger et al.[34] collected time dependent FTIR spectra to monitor variations in ν_{as} (UO_2^{2+}) within hematite suspensions containing U(VI) and Fe(II), thereby elucidating the reductive transformation of surface-associated U(VI) to U(IV), facilitated by Fe(II).

In our earlier study, we developed a cost-effective and environmentally sustainable nanomaterial, PCNCFH, which exhibited a high uranium adsorption capacity of 100 mg/g for the remediation of uranium-contaminated drinking water.[35] The material was synthesized by functionalizing cellulose with a phosphorylating agent, sodium trimetaphosphate (STMP), followed by the incorporation of iron oxyhydroxide onto the cellulose matrix. The introduction of phosphorus-containing functional groups enhances the adsorption performance, as uranium, a hard Lewis acid, exhibits strong affinity toward hard Lewis base functionalities such as phosphate, carboxyl, phosphonate, amino, and other oxygen- and nitrogen-donor groups.[36,37] Comprehensive investigations, including comparative performance analysis with other adsorbents, physicochemical characterization, batch adsorption studies, regeneration, mechanical stability assessments, as well as postadsorption characterization, were reported therein.

Building upon this foundation, the present work addresses a critical and, to the best of our knowledge, previously unexplored aspect: the species-specific adsorption kinetics of environmentally prevalent uranyl complexes on PCNCFH surfaces, analyzed using Raman spectroscopy. Specifically, we examine the adsorption behavior of $UO_2(CO_3)_3^{4-}$, $UO_2(CO_3)_2^{2-}$, and $(UO_2)_3(OH)_5^+$ - the dominant aqueous uranyl species within natural water systems in the range of pH 5−10. Our Raman spectroscopic investigations reveal a distinct and systematic trend: $UO_2(CO_3)_3^{4-}$ exhibits markedly slower adsorption kinetics compared with the other species across all studied pH values (5.0, 7.5, and 9.0). This observation, further supported by complementary theoretical calculations, provides new mechanistic insights into species-dependent interaction pathways between uranyl complexes and PCNCFH. IR spectroscopy also confirms the presence of specific uranyl species at the corresponding pH values. The kinetic profiles have been quantitatively modeled using established adsorption kinetic frameworks, further enhancing the predictive relevance and applicability of these findings.

EXPERIMENTAL SECTION

Sample Preparation

PCNCFH was synthesized following the procedure reported in our previous study.[35] The sample preparation procedure was adapted with minor modifications from the method reported by Lu et al. to avoid precipitation during pH adjustment.[33] Stock solutions of 0.1 M UO_2^{2+} and 0.5 M Na_2CO_3 were prepared, with the uranyl solution prepared using $UO_2(NO_3)_2{\cdot}6H_2O$(s). Samples were prepared by mixing 0.1 M

https://doi.org/10.1021/acs.langmuir.6c00300
Langmuir 2026, 42, 11219−11228

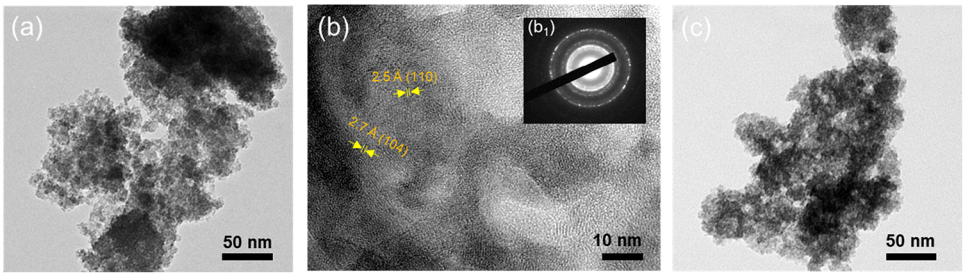

Figure 1. (a) HRTEM image of PCNCFH. (b) Lattice resolved image of PCNCFH with a fast Fourier-transform of the image (inset b_1). (c) HRTEM image of U-PCNCFH.

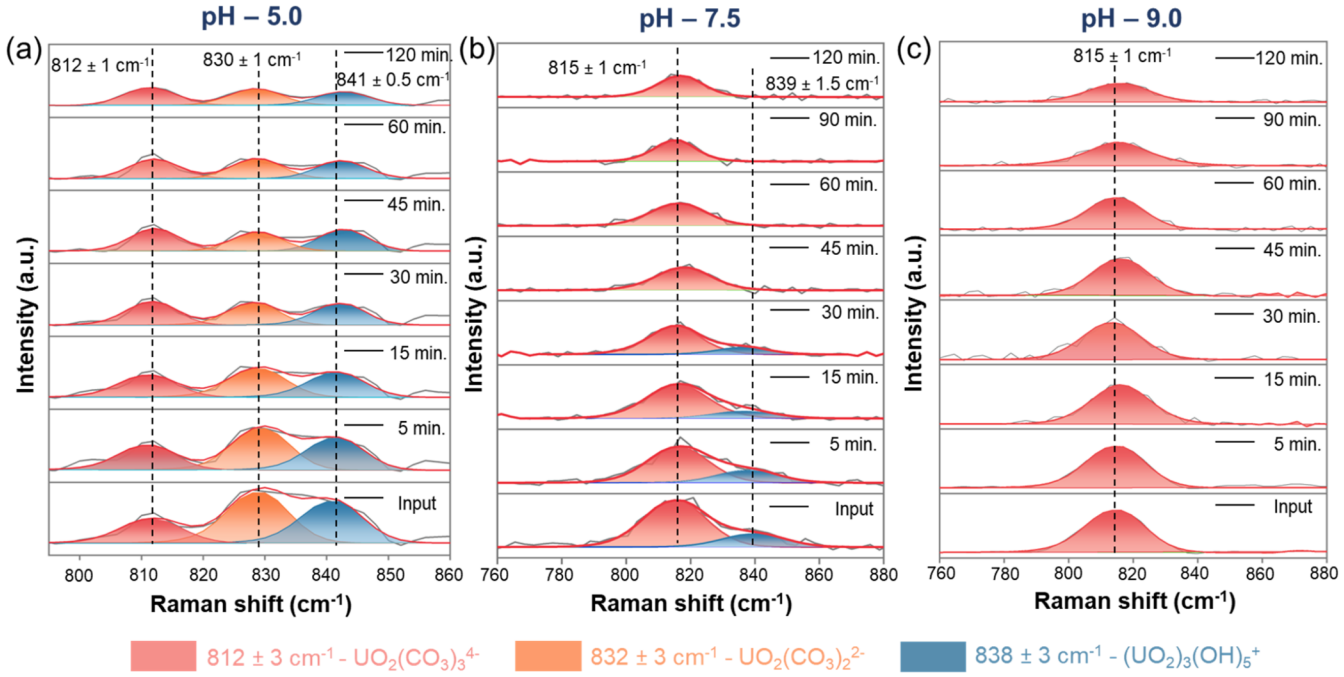

Figure 2. Time-dependent Raman spectra of the interaction of PCNCFH with U(VI) at (a) pH 5.0, (b) pH 7.5, and (c) pH 9.0. Mass of the adsorbent: 750 mg. All the Raman spectra were deconvoluted using CasaXPS software.[38]

UO_2^{2+} and 0.5 M Na_2CO_3 to achieve a final $[CO_3^{2-}]/[UO_2^{2+}]$ ratio of 3.5. The pH was adjusted to 5.0, 7.5, and 9.0 by dropwise addition of 0.2 M HNO_3, and the final volume was maintained constant for all samples. The uranyl solution was allowed to equilibrate for 30 min prior to the addition of the adsorbent or any subsequent experiments. For time-dependent Raman studies, the final volume was fixed at 15 mL, whereas for concentration-dependent Raman calibration, a total volume of 5 mL was used.

For adsorption kinetics studies, 4.5 mL of 0.1 M UO_2^{2+} solution was mixed with 3.15 mL of 0.5 M Na_2CO_3 (initial pH - 10.3−10.5), and the remaining volume was adjusted using deionized water and 0.2 M HNO_3 to achieve the desired pH. Under these conditions, the final UO_2^{2+} concentration was 0.03 M. PCNCFH (750 mg to 2.5 g) was added to 15 mL of the prepared uranyl solution in a 30 mL reaction vessel, and the suspension was continuously stirred using a magnetic stirrer. Aliquots of 0.5 mL were collected at various time intervals of 5, 15, 30, 45, 60, 90, and 120 min, followed by immediate centrifugation. Any solid residue obtained was discarded, and Raman measurements were performed on the supernatant.

For IR measurements, the initial uranyl solution was prepared following the same procedure as that used for the time-dependent Raman analysis.

For concentration-dependent Raman calibration, 1.5 mL of 0.1 M UO_2^{2+} solution was mixed with 1.05 mL of 0.5 M Na_2CO_3 (initial pH 10.3−10.5), and the final volume (5 mL) was adjusted using deionized water of respective pH and 0.2 M HNO_3 to achieve the desired pH.

For ζ-potential measurements, deionized water samples with pH values ranging from 5 to 10 were first prepared by using 1 M Na_2CO_3 and 1 M HNO_3. Subsequently, 2 mg of PCNCFH was dispersed in 2 mL of deionized water at the respective pH. The pH of each dispersion was then rechecked and adjusted, if necessary, to the desired value prior to measurement.

Details of the materials, characterization techniques, and computational details are provided in the Supporting Information.

RESULTS AND DISCUSSION

Figure 1a,c represent the high-resolution transmission electron microscopy (HRTEM) images of PCNCFH before and after uranium adsorption (samples after U(VI) adsorption are labeled as U-PCNCFH). In both cases, the material predominantly exhibits an amorphous structure, which remains stable under ambient conditions, even after prolonged exposure to U(VI)-spiked water. However, upon continuous electron beam irradiation of 20−25 min, distinct lattice fringes become apparent [Figure 1b], indicative of beam-induced crystallization arising from the gradual transformation of ferrihydrite into its thermodynamically more stable phase, hematite. The corresponding fast Fourier transform (FFT)

https://doi.org/10.1021/acs.langmuir.6c00300
Langmuir 2026, 42, 11219−11228

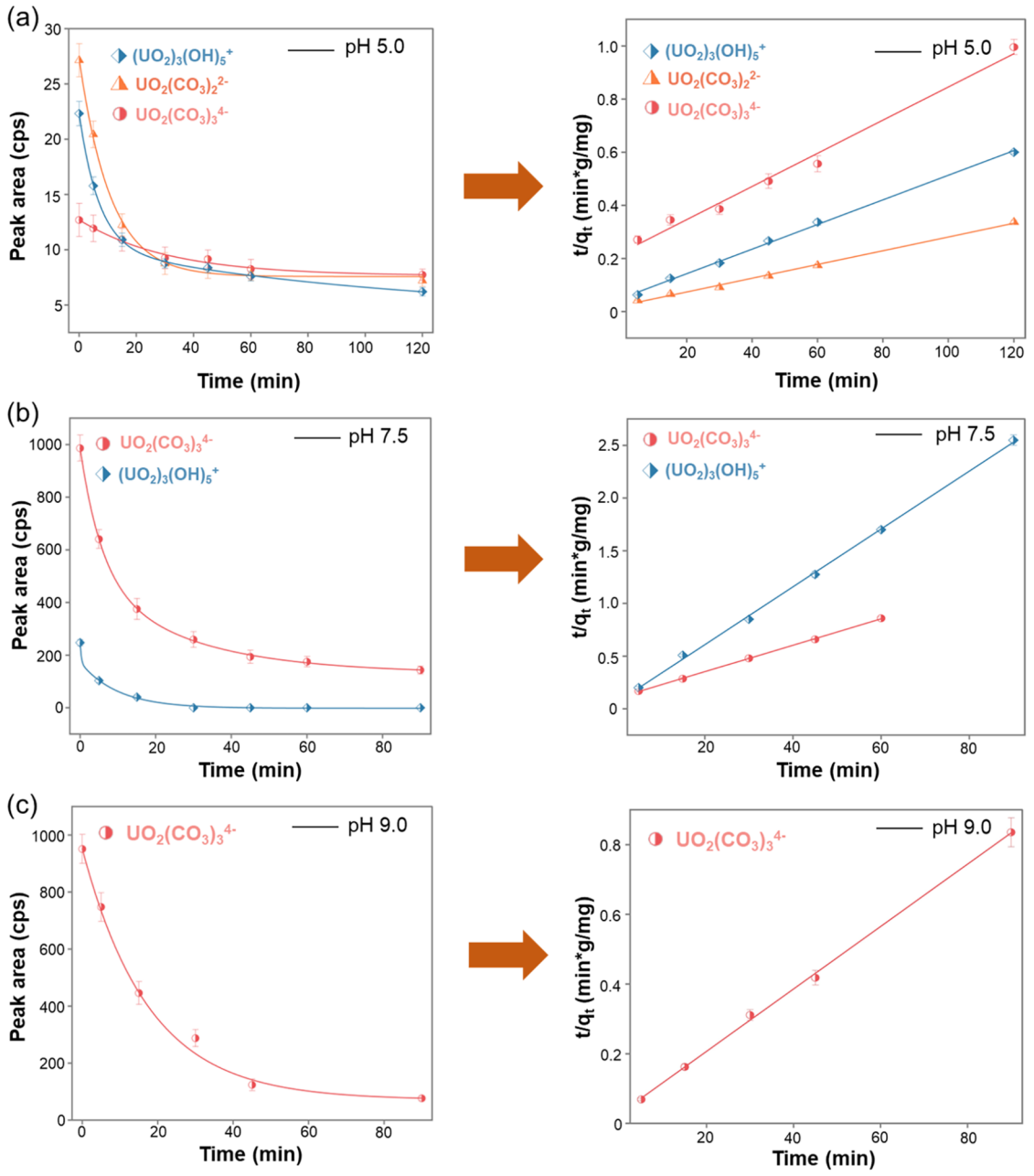

Figure 3. Peak area vs time graph and pseudo-second-order kinetics graph for PCNCFH at (a) pH 5.0, (b) pH 7.5, and (c) pH 9.0.

pattern is shown in inset b_1. The lattice planes of hematite observed in the process are marked.

To understand the adsorption kinetics of different uranyl species on PCNCFH, time-dependent Raman studies were performed at three pH values (5.0, 7.5, and 9.0). Figure 2a–c represent the time-dependent Raman studies of uranyl species at pH 5.0, 7.5, and 9.0, respectively. At pH 5.0, the spectra indicate the presence of three U(VI) species $UO_2(CO_3)_3^{4-}$, $UO_2(CO_3)_2^{2-}$, and $(UO_2)_3(OH)_5^{+}$ exhibiting characteristic Raman peaks (ν_1(symmetric)) at 812 cm^{-1}, 830 cm^{-1}, and 841 cm^{-1}, respectively. At pH 7.5, two species dominate: $UO_2(CO_3)_3^{4-}$ at 815 cm^{-1} and $(UO_2)_3(OH)_5^{+}$ at 839 cm^{-1}. Under alkaline conditions (pH of 9.0), $UO_2(CO_3)_3^{4-}$ emerges as the dominant species, exhibiting a Raman frequency at 815 cm^{-1}. The existence of this species was further confirmed by IR spectroscopy of the corresponding input solutions at each pH (Figure S1). FT-IR analysis reveals a characteristic peak (ν_3(asymmetric)) at 890 cm^{-1} in the spectra of stock solutions at pH 7.5 and 9.0, which confirms the presence of the $UO_2(CO_3)_3^{4-}$ complex. A second peak at 923 cm^{-1} appears at pH 7.5, indicating the presence of $(UO_2)_3(OH)_5^{+}$. In contrast, the spectrum at pH 5.0 exhibits a clear shift, with a peak emerging at 947 cm^{-1}, confirming the formation of hydroxo-uranyl complexes.[26] To further verify the adsorption of uranyl species, FT-IR spectra of PCNCFH were recorded before and after U(VI) species adsorption at pH 7.5 (Figure S2). After adsorption, a prominent band at ∼ 903 cm^{-1} is observed, which is attributed to the asymmetric stretching vibration of U–O in ferrihydrite surface-bound U(VI) hydroxo complexes.[32] This observation suggests the preferential adsorption of hydroxo–uranyl species over carbonate complexes at pH 7.5. Time-dependent Raman spectra for pH 7.5 and 9.0 were

https://doi.org/10.1021/acs.langmuir.6c00300
Langmuir 2026, 42, 11219–11228

Table 1. Adsorption Data in Terms of Rate Constants (k), Uptake of U(VI) at Equilibrium (q_e), and Initial Rates (h)

pH	adsorbent (g)	species	q_e (mg/g)	rate constant (k) (min(mg/g))$^{-1}$	initial rate (mg/g (min)$^{-1}$), $h = kq_e^2$	coefficient of determination, R^2
5.0	0.75	$UO_2(CO_3)_3^{4-}$	166.25	17.60×10^{-5}	4.86	0.987
		$UO_2(CO_3)_2^{2-}$	387.59	30.0×10^{-5}	45.06	0.996
		$(UO_2)_3(OH)_5^+$	215.51	43.35×10^{-5}	20.13	0.998
7.5	2.5	$UO_2(CO_3)_3^{4-}$	74.18	304.10×10^{-5}	16.73	0.999
		$(UO_2)_3(OH)_5^+$	35.99	1976.79×10^{-5}	25.60	0.999
9.0	2.5	$UO_2(CO_3)_3^{4-}$	98.42	1214.43×10^{-5}	117.63	0.998

collected using a 633 nm excitation source. At pH 5.0, the Raman spectrum with 633 nm excitation showed distinct fluorescence, limiting Raman measurements.[33] Therefore, the spectrum was measured with 785 nm excitation, which exhibited 3 distinct features, of which two ($UO_2(CO_3)_3^{4-}$ and $(UO_2)_3(OH)_5^+$) were observed with 633 nm as well. To ensure consistency between the two excitation wavelengths, we remeasured the spectra of stock solutions at pH 7.5 and 9.0 using 785 nm excitation. A comparison of these spectra is presented in Figure S3, demonstrating good agreement between the spectra obtained using both the excitations. The intensities of various uranyl species progressively decreased upon interaction with PCNCFH with time, at 5.0, 7.5, and 9.0 pH, as shown in Figure 2. These results indicate that the uranyl species present at a given pH in solution remain unchanged during adsorption. In all cases, the $UO_2(CO_3)_3^{4-}$ species exhibited a slower decrease in intensity compared to the other two complexes. Additionally, the $(UO_2)_3(OH)_5^+$ species displayed markedly faster adsorption kinetics than the remaining species under both neutral and acidic conditions.

To determine the adsorption rate constants of the uranyl species at each pH, concentration-dependent Raman measurements were performed on solutions prepared at the corresponding pH values. The Raman spectra obtained at varying concentrations, along with the resulting correlation between the peak area and U(VI) concentration for pH 5.0, are shown in Figure S4a,b, respectively. Similar data are presented in Figures S5 and S6 for pH 7.5 and 9.0, respectively. To ensure that the adsorption process reached saturation, the amount of PCNCFH was increased from 750 mg to 2.5 g for the experiments conducted at pH 7.5 and 9.0, whereas 750 mg was sufficient to achieve saturation within 2 h at pH 5.0. The time-dependent Raman analysis data for pH 7.5 and pH 9.0, obtained using 2.5 g of PCNCFH, are presented in Figure S7a,b, respectively. Using the slope and intercept values obtained from the concentration-correlation plots, the time-dependent unknown concentrations of the individual uranyl species were calculated for all pH values using eq 1 in the Supporting Information. To better understand the adsorption behavior, the kinetic data were analyzed using two models: Lagergren's pseudo-first-order (Figure S8 and eq 3 in the Supporting Information) and Ho's pseudo-second-order (Figure 3 and eq 2 in the Supporting Information).[39] The pseudo-second-order model exhibited a higher correlation coefficient (R^2) compared with the pseudo-first-order model, indicating a better fit to the experimental data. Accordingly, the adsorption kinetics were further evaluated using the pseudo-second-order model by constructing a plot of t/q_t versus t (Figure 3). q_t values were calculated using eq 4 in the Supporting Information. Figure 3a–c represent the peak area vs time graph and the corresponding pseudo-second order kinetics plot for pH 5.0, 7.5, and 9.0, respectively. The rate constants (k) and equilibrium adsorption capacities (q_e) were determined by using the slopes and intercepts of the linear fits. The extracted parameters are summarized in Table 1.

Adsorption Mechanism at Acidic and Neutral pH

The slower adsorption kinetics and higher q_e of $UO_2(CO_3)_3^{4-}$ compared to other uranyl species such as $UO_2(CO_3)_2^{2-}$ and $(UO_2)_3(OH)_5^+$ on PCNCFH can be explained by charge interactions, surface complexation mechanisms, and structural constraints at the adsorbent interface. At neutral pH, PCNCFH presents surface functionalities such as $Fe^{3+}-O^{2-}$ (from ferrihydrite) and C–OH (from cellulose). From the ζ-potential data of PCNCFH (Figure S9), it is observed that the surface charge of PCNCFH is −27.6 mV at pH 7.5. Owing to this negatively charged surface, the cationic species $(UO_2)_3(OH)_5^+$ readily interacts with PCNCFH via an inner-sphere complexation mechanism under neutral conditions. This results in accelerated adsorption kinetics due to strong electrostatic attraction. In contrast, $UO_2(CO_3)_3^{4-}$, being highly anionic, experiences electrostatic repulsion from the negatively charged PCNCFH surface, which slows its initial uptake. A similar trend was observed at pH 5.0, where PCNCFH carries a surface charge of −13.4 mV. This negative charge mainly arises from the sodium phosphate ($-PO_4^-Na^+$) groups grafted onto the cellulose backbone. At mildly acidic pH, these phosphate groups remain partially deprotonated, even the overall surface charge of bare cellulose ferrihydrite is positive.[40−42] Due to the negatively charged surface of PCNCFH, the cationic species $(UO_2)_3(OH)_5^+$ binds more strongly through electrostatic attraction than the two negatively charged uranyl carbonate species. As a result, at pH 5.0, the adsorption kinetics follow the order: $(UO_2)_3(OH)_5^+$ > $UO_2(CO_3)_2^{2-}$ (less negative charge) > $UO_2(CO_3)_3^{4-}$ (more negative charge).

The q_e defined as the amount adsorbed per unit mass depends on the quantity of uranyl species that can bind on the surface and on the number of available active sites. Because $(UO_2)_3(OH)_5^+$ is a polynuclear hydroxo cluster, it tends to form bidentate or tridentate surface complexes rather than simple monodentate binding. Based on the crystal radii of uranyl ions, the adsorbed $(UO_2)_3(OH)_5^+$ cluster occupies an estimated cross-sectional diameter of 0.6–0.8 nm on the ferrihydrite surface, whereas the area associated with a single surface (FeOH) functional group is only about 0.05 nm^2.[43] The surface reactions describing the interaction of $(UO_2)_3(OH)_5^+$ with ferrihydrite can therefore be expressed as follows:

$$2(FeOH)\,(s) + 3UO_2^{2+}\,(aq) + 5H_2O \rightleftharpoons \begin{matrix} FeO^- \\ FeO^- \end{matrix}\!\!\diagup\!\!\diagdown (UO_2)_3(OH)_5^+ + 7H^+\,(ad) \quad \text{(i)}$$

$$3(FeOH)\,(s) + 3UO_2^{2+}\,(aq) + 5H_2O \rightleftharpoons \begin{matrix} FeO^- \\ FeO^- \\ FeO^- \end{matrix}\!\!\diagup\!\!\diagdown\!\!\diagup (UO_2)_3(OH)_5^+ + 8H^+\,(ad) \quad \text{(ii)}$$

https://doi.org/10.1021/acs.langmuir.6c00300
Langmuir 2026, 42, 11219−11228

Because the $(UO_2)_3(OH)_5^+$ cluster occupies a large surface footprint on PCNCFH, only a limited number of these units can bind per unit area. Under neutral conditions, its lower fractional abundance further restricts the number of available complexes for adsorption, leading to a reduced q_e value. In contrast, $UO_2(CO_3)_2^{2-}$ and $UO_2(CO_3)_3^{4-}$ can form multiple ternary complexes with ferrihydrite surface sites, allowing more efficient packing and higher uptake.[44] The overall adsorption process is therefore supported by the following surface complexation reactions.

$$FeOH(s) + UO_2^{2+}(aq) + 2CO_3^{2-}(aq) + H^+(aq) \rightleftharpoons [FeOH_2^+\text{-}UO_2(CO_3)_2^{2-}] \quad \text{(iii)}$$

$$FeOH(s) + UO_2^{2+}(aq) + 3CO_3^{2-}(aq) + H^+(aq) \rightleftharpoons [FeOH_2^+\text{-}UO_2(CO_3)_3^{4-}] \quad \text{(iv)}$$

At acidic pH, Raman analysis of the stock solution indicates that $(UO_2)_3(OH)_5^+$ is the predominant species, where $UO_2(CO_3)_3^{4-}$ occurs only in minor fractions. The greater availability of the hydroxo-bridged complex partly accounts for its higher q_e compared to those of the carbonate species. However, its relatively large molecular footprint limits the surface packing on PCNCFH, which moderates the difference in q_e between the two. $UO_2(CO_3)_2^{2-}$, being structurally smaller, occupies less surface area and can adsorb more densely under acidic conditions. Its relatively higher abundance at this pH further enhances its overall uptake. Consequently, at pH 5.0, the equilibrium capacities follow the order: $UO_2(CO_3)_2^{2-}$ (387.59 mg/g) > $(UO_2)_3(OH)_5^+$ (215.51 mg/g) > $UO_2(CO_3)_3^{4-}$ (166.25 mg/g). Overall, the observed order of rate constants and equilibrium capacities reflects a consistent picture: electrostatic and kinetic factors control the initial uptake rate, whereas the species abundance, binding configuration, and surface footprint govern the final equilibrium capacity.

Effect of Competing Ions in Groundwater Systems

In natural groundwater systems, the presence of competing ions can influence uranyl adsorption behavior. Common interfering ions include Ca^{2+}, Mg^{2+}, and HCO_3^-. Previous studies[43] have shown that Ca^{2+} and Mg^{2+} at concentrations of $\sim 10^{-3}$ M do not significantly affect U(VI) adsorption on ferrihydrite. In contrast, bicarbonate plays a more crucial role by forming stable uranyl−carbonate complexes (e.g., UO_2CO_3, $UO_2(CO_3)_3^{4-}$ and $UO_2(CO_3)_2^{2-}$), which exhibit lower affinity toward the adsorbent surface and compete for available binding sites, particularly at intermediate pH. Wazne et al.[45] reported that in the presence of carbonate (introduced as $NaHCO_3$), aqueous uranyl carbonate complexes predominate at pH > 5.0. At higher pH, carbonate further increases the solubility of U(VI), thereby reducing adsorption efficiency. Additionally, the presence of carbonate and U(VI) leads to a decrease in the ζ-potential of iron oxyhydroxides, suggesting that uranyl is predominantly adsorbed in anionic forms under these conditions.

DFT Investigations

Under environmentally relevant oxidative and thermal conditions, iron oxyhydroxides like goethite (FeOOH) convert to hematite (α-Fe_2O_3), the most stable anhydrous iron oxide. FeOOH can therefore be considered as a hydrated precursor whose long-term product is Fe_2O_3.[46−48] Additionally, ferrihydrite exhibits poor crystallinity and significant structural disorder, posing challenges in constructing a reliable atomistic model for DFT calculations.[49] Therefore, to represent the stable iron-oxide framework governing uranyl binding and consistent with common practice in first-principles modeling, DFT calculations in this work were performed on α-Fe_2O_3 surfaces instead of FeOOH. Because ferrihydrite is the primary component responsible for U(VI) adsorption in PCNCFH, DFT calculations were carried out to evaluate the adsorption energies of the uranyl species on iron oxide surfaces. The corresponding experimental comparison of U(VI) removal efficiencies between phosphorylated cellulose nanocrystals (PCNC) and PCNCFH is provided in Table S1.

Hematite (α-Fe_2O_3) is a thermodynamically stable iron oxide having a hexagonal corundum-type structure (space group $R\bar{3}c$). We conducted calculations for both ferromagnetic and antiferromagnetic spin configurations, and in agreement with previous computational results, we found the antiferromagnetic configuration to be the most stable one.[50−52] Based on these results, we took the hexagonal antiferromagnetic α-Fe_2O_3 structure, with the spin configuration illustrated in Figure S10a. The α-$Fe_2O_3(0001)$ facet is one of the most dominant and extensively studied surfaces of α-Fe_2O_3.[53] Studies have shown that the stability of the α-$Fe_2O_3(0001)$ surface depends strongly on its chemical termination. Earlier theoretical and experimental investigations under ultrahigh vacuum (UHV) conditions have suggested that the Fe-terminated surface (Fe−O_3−Fe−R) is the most stable among the clean stoichiometric terminations.[54,55] Based on these findings, this Fe-terminated configuration was adopted for constructing the α-$Fe_2O_3(0001)$ slab used in our adsorption studies. A nine-layer slab model of α-$Fe_2O_3(0001)$ was constructed from the optimized bulk structure (Figure S10c). Upon structural relaxation, the topmost Fe atoms were observed to move toward the underlying oxygen layer (Figure S10b,d), in agreement with the surface relaxations reported in previous literature.[55] To preserve bulk-like characteristics, the bottom three atomic layers of the slab were constrained to their bulk positions, whereas the remaining layers and any adsorbed species were fully relaxed.

The structural coordinates of both uranium complexes were taken from previous studies and further optimized.[56,57] Based on combined DFT and EXAFS analyses, Tsushima et al.[56] demonstrated that $[(UO_2)_3(OH)_5]^+$ in aqueous solution is better described as $[(UO_2)_3(O)(OH)_3]^+$ featuring a central oxo bridging group. Other studies have also suggested that the complex commonly described as $[(UO_2)_3(OH)_5]^+$ may be, in fact, $[(UO_2)_3(O)(OH)_3]^+$.[58,59] Notably, these two formulations are indistinguishable in potentiometric titrations, as both correspond to the loss of five protons.[56,60] Accordingly, we considered the $[(UO_2)_3(O)(OH)_3(H_2O)_6]^+$ structure, which has been reported as the most stable isomer of $[(UO_2)_3(O)(OH)_3]^+$.[56] The optimized geometries of $[UO_2(CO_3)_3]^{4-}$ and $[(UO_2)_3(O)(OH)_3(H_2O)_6]^+$ are given in Figure S11.

To examine the binding energy of these uranium complexes, we placed them on an optimized 4 × 4 supercell of α-Fe_2O_3 and further optimized these entire systems. The optimized geometries of uranium complexes adsorbed onto the α-Fe_2O_3 surface are shown in Figure S12. Since each uranium complex can bind to the surface in multiple configurations, we conducted additional ab initio molecular dynamics (AIMD) simulations for approximately 2.5 ps to identify the feasible

https://doi.org/10.1021/acs.langmuir.6c00300
Langmuir 2026, 42, 11219−11228

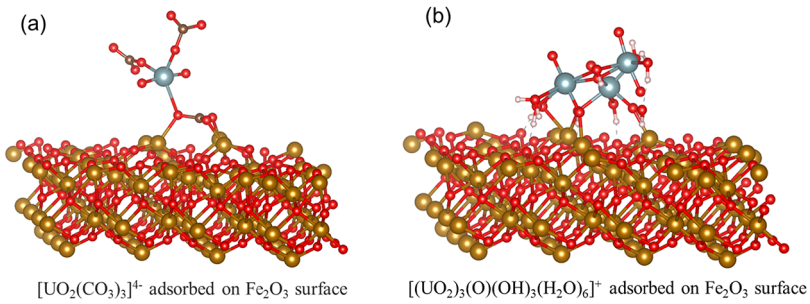

Figure 4. Optimized geometries obtained by fully relaxing the lowest-energy configurations extracted from the NVT simulations: (a) $[UO_2(CO_3)_3]^{4-}$ and (b) $[(UO_2)_3(O)(OH)_3(H_2O)_6]^+$ adsorbed onto the α-$Fe_2O_3(0001)$ surface.

low-energy configurations. We started these NVT simulations from the optimized geometries of the entire system. In Figure S13, we presented the variations in the potential energy during these simulations. The corresponding lowest-energy configurations, after subsequent optimization, are shown in Figure 4. For the hydroxo complex $[(UO_2)_3(O)(OH)_3(H_2O)_6]^+$ (Figure 4b), strong interactions are observed between surface Fe atoms and the oxygen atoms of the complex, along with additional hydrogen bonding between surface oxygen atoms and hydrogen atoms of both the coordinated H_2O molecules and the OH^- groups. In contrast, the carbonate complex $[UO_2(CO_3)_3]^{4-}$ (Figure 4a) exhibits noticeable distortion upon adsorption, accompanied by Fe−O interfacial interactions.

Next, we computed the binding energies of these lowest-energy structures by employing the Hubbard corrections with a Hubbard U value of 5 eV for iron and 0 eV for uranium atoms (as explained in computational details). Our calculations show that the hydroxo complex, i.e., $[(UO_2)_3(O)(OH)_3(H_2O)_6]^+$ binds to the surface strongly (−9.71 eV) than the $[UO_2(CO_3)_3]^{4-}$ complex (−8.93 eV), in agreement with our experimental observations (the $(UO_2)_3(OH)_5^+$ species exhibits significantly faster adsorption kinetics, with a rate constant of 1976.79×10^{-5} $(\text{min}(\text{mg/g}))^{-1}$, compared to the $[UO_2(CO_3)_3]^{4-}$ complex with rate constant of 304.10×10^{-5} $(\text{min}(\text{mg/g}))^{-1}$). However, we acknowledge that binding energies do not directly determine kinetic rate constants, as adsorption kinetics are also governed by factors such as activation barriers, diffusion, and speciation-dependent transport processes. In this work, the DFT calculations are therefore intended to provide qualitative support for the experimental observations rather than to establish a direct quantitative correlation between the thermodynamic and kinetic parameters. Binding energies computed with different Hubbard U values (Table S2) show the same qualitative trend. The enhanced binding energy of the $[(UO_2)_3(O)(OH)_3(H_2O)_6]^+$ is likely due to the greater number of Fe−O interactions, combined with additional stabilization provided by hydrogen bonding, which collectively strengthens its affinity to the surface.

CONCLUSIONS

Species-dependent uranium adsorption on PCNCFH was investigated by Raman spectroscopy. Time-dependent Raman analysis helped us to understand the kinetics and adsorption capacity of individual uranyl species on PCNCFH at different pH. Specifically, we examine the adsorption behavior of $UO_2(CO_3)_3^{4-}$, $UO_2(CO_3)_2^{2-}$, and $(UO_2)_3(OH)_5^+$ − the dominant aqueous uranyl species within natural water systems at pH 5−10. This study reveals a distinct and systematic trend: $UO_2(CO_3)_3^{4-}$ exhibits markedly slower adsorption kinetics compared to the other species across all studied pH values (5.0, 7.5, and 9.0). This observation, rigorously validated by complementary IR spectroscopic analyses and theoretical calculations, provides new mechanistic insight into species-dependent interaction pathways between uranyl complexes and PCNCFH. The kinetic profiles have been quantitatively modeled using established adsorption kinetic frameworks. Overall, this study concluded that the observed order of rate constants and equilibrium capacities reflects a consistent picture: electrostatic and kinetic factors control the initial uptake rate, while the mode of binding controls the equilibrium capacity. These findings provide mechanistic insight into species-specific uranyl uptake on PCNCFH, offering a framework for designing species-targeted and pH-optimized uranium remediation materials.

ASSOCIATED CONTENT

Supporting Information

The Supporting Information is available free of charge at https://pubs.acs.org/doi/10.1021/acs.langmuir.6c00300.

Materials; instrumentation; computational details; comparative FTIR spectra of uranyl stock solutions at pH 5.0, 7.5 and 9.0; FTIR spectra of PCNCFH and U-PCNCFH at pH 7.5; comparative Raman spectral peak fitting analyses for the uranyl solution collected at λ_{ex} = 633 and 785 for pH 7.5, and pH 9.0; Raman spectra for the various concentrations of U(VI) stock solutions at pH 5.0 and its corresponding peak area vs concentration graph; Raman spectra for the various concentrations of U(VI) stock solutions at pH 7.5 and its corresponding peak area vs concentration graph; Raman spectra for the various concentrations of U(VI) stock solutions at pH 9.0 and its corresponding peak area vs concentration graph; time-dependent Raman spectra of the interaction of PCNCFH with U(VI) at pH 7.5 and pH 9.0; pseudo-first-order kinetics graph for PCNCFH at pH 5.0, pH 7.5, and pH 9.0; ζ-potential as a function of pH (range 5−10) for PCNCFH particles in water; bulk hexagonal conventional unit cell (containing 6 formula units) of α-Fe_2O_3; Top and side views of the optimized $[UO_2(CO_3)_3]^{4-}$ complex and $[(UO_2)_3(O)(OH)_3(H_2O)_6]^+$ complex; side views of the optimized $[UO_2(CO_3)_3]^{4-}$ and $[(UO_2)_3(O)(OH)_3(H_2O)_6]^+$ complexes adsorbed onto the α-$Fe_2O_3(0001)$ surface; energy profiles of $[UO_2(CO_3)_3]^{4-}$ and $[(UO_2)_3(O)(OH)_3(H_2O)_6]^+$ complexes adsorbed onto the α-

https://doi.org/10.1021/acs.langmuir.6c00300
Langmuir 2026, 42, 11219−11228

$Fe_2O_3(0001)$ surface; comparative U(VI) removal efficiency of PCNC and PCNCFH, calculated from ICPMS data; binding energies with varying Hubbard *U* values for uranium complexes on α-$Fe_2O_3(0001)$; equations used in the main text; references (PDF)

AUTHOR INFORMATION

Corresponding Authors

Sharma S. R. K. C. Yamijala − *Department of Chemistry, Indian Institute of Technology Madras, Chennai 600036, India*; Email: yamijala@smail.iitm.ac.in

Thalappil Pradeep − *DST Unit of Nanoscience (DST UNS) and Thematic Unit of Excellence (TUE), Department of Chemistry, Indian Institute of Technology Madras, Chennai 600036, India*; orcid.org/0000-0003-3174-534X; Email: pradeep@iitm.ac.in

Authors

Tanmayaa Nayak − *DST Unit of Nanoscience (DST UNS) and Thematic Unit of Excellence (TUE), Department of Chemistry, Indian Institute of Technology Madras, Chennai 600036, India*

Sujan Manna − *DST Unit of Nanoscience (DST UNS) and Thematic Unit of Excellence (TUE), Department of Chemistry, Indian Institute of Technology Madras, Chennai 600036, India*

Ankita Narwal − *Department of Chemistry, Indian Institute of Technology Madras, Chennai 600036, India*

Bijesh Kumar Malla − *DST Unit of Nanoscience (DST UNS) and Thematic Unit of Excellence (TUE), Department of Chemistry, Indian Institute of Technology Madras, Chennai 600036, India*; orcid.org/0009-0005-1148-0884

Sonali Seth − *DST Unit of Nanoscience (DST UNS) and Thematic Unit of Excellence (TUE), Department of Chemistry, Indian Institute of Technology Madras, Chennai 600036, India*

Sandeep K. Reddy − *Centre for Computational and Data Science, Indian Institute of Technology Kharagpur, Kharagpur 721302 West Bengal, India*; orcid.org/0000-0002-1458-6853

Complete contact information is available at: https://pubs.acs.org/10.1021/acs.langmuir.6c00300

Notes

The authors declare no competing financial interest.

ACKNOWLEDGMENTS

T.N. thanks the Ministry of Human Resource Development, Government of India, for a senior research fellowship. T.P. acknowledges financial support from SERB SUPRA (Grant SPR/2021/000439), Centre of Excellence on Molecular Materials and Functions under the Institution of Eminence scheme of IIT Madras and JC Bose Fellowship. S.S.R.K.C.Y. acknowledges the financial support from Anusandhan National Research Foundation (ANRF/ARG/2025/009797/CS). The authors also acknowledge the Department of Science and Technology, Government of India for supporting our research program on nanomaterials over the past two decades.

REFERENCES

(1) Zhang, J.; Jiang, Y.; You, M.; Zhao, J.; Xue, S.; Fang, H.; Wei, Y.; Sun, Z.; Zeng, T.; Wan, Z.; Xu, M.; Hu, Y. Polydopamine-Modified Coal Fly Ash Composite Electrodes for Improved Electroadsorption of Uranium. *J. Water Process Eng.* **2025**, *72*, No. 107612.

(2) Uranium Occurence In Shallow Aquifer In India 2020 https://www.cgwb.gov.in/old_website/WQ/URANIUM_REPORT_2019-20.pdf.

(3) Rani, N.; Singh, P.; Kumar, S.; Kumar, P.; Bhankar, V.; Kamra, N.; Kumar, K. Recent Advancement in Nanomaterials for the Detection and Removal of Uranium: A Review. *Environ. Res.* **2023**, *234*, No. 116536.

(4) Smedley, P. L.; Kinniburgh, D. G. Uranium in Natural Waters and the Environment: Distribution, Speciation and Impact. *Appl. Geochem.* **2023**, *148*, No. 105534.

(5) Shvareva, T. Y.; Fein, J. B.; Navrotsky, A. Thermodynamic Properties of Uranyl Minerals: Constraints from Calorimetry and Solubility Measurements. *Ind. Eng. Chem. Res.* **2012**, *51* (2), 607−613.

(6) Murphy, W. M.; Shock, E. L. Environmental Aqueous Geochemistry of Actinides. In *Uranium*; Burns, P. C.; Finch, R. J., Eds.; De Gruyter, 1999; Chapter 5, pp 221−254.

(7) Burns, P. C. U^{6+} minerals and inorganic compounds: insights into an expanded structural hierarchy of crystal structures. *Can. Mineral.* **2005**, *43* (6), 1839−1894.

(8) Zhang, N.; Li, W.; Li, J.; Wang, Q.; Li, B.; Zhang, J.; Zhang, T.; Li, Z.; Li, Y.; Tian, B.; Zhao, H. Chemically and Physically Dual Cross-Linked Phosphorylated Cellulose Hydrogel for Uranium Removal from Aqueous Solution. *Sep. Purif. Technol.* **2025**, *368*, No. 132907.

(9) Li, Z.; Yan, L.; Luo, W.; Liao, X.; Shi, B. Ultrafast Uranium Capture via Phthalocyanine-Functionalized Collagen Fibers: Toward Efficient Nuclear Wastewater Remediation. *ACS EST Water* **2025**, *5* (12), 7560−7570.

(10) Seth, S.; Islam, M. R.; Nayak, T.; Kini, A. R.; Manna, S.; Malla, B. K.; Nagar, A.; Pradeep, T. Enhanced U(VI) Removal from Groundwater Using Amide-Functionalized Biopolymer-Based Adsorbent for a Practical Solution. *ACS Sustainable Chem. Eng.* **2025**, *13*, 10918.

(11) Camacho, L. M.; Deng, S.; Parra, R. R. Uranium Removal from Groundwater by Natural Clinoptilolite Zeolite: Effects of pH and Initial Feed Concentration. *J. Hazard. Mater.* **2010**, *175* (1−3), 393−398.

(12) Hassan, S. S. M.; Abdel Rahman, E. M.; El-Subruiti, G. M.; Kamel, A. H.; Diab, H. M. Removal of Uranium-238, Thorium-232, and Potassium-40 from Wastewater via Adsorption on Multiwalled Carbon Nanotubes. *ACS Omega* **2022**, *7* (14), 12342−12353.

(13) Musa, H.; Alnasra, O.; Khalili, F. Innovative Study on the Removal of Thorium(IV) and Uranium(VI) Ions from Aqueous Solutions via Oak-Derived Charcoal: Kinetic Analysis and Adsorptive Performance. *J. Radioanal. Nucl. Chem.* **2025**, *334*, 4933.

(14) Zhou, T.; Guo, Y.; Zeng, Z.; Wang, Z.; Liu, X.; Li, H. ZIF-67-Embedded Polyacrylamide/Sodium Alginate/Polyacrylic Acid Hydrogel for Efficient and Selective Uranium Extraction. *ACS Appl. Mater. Interfaces* **2025**, *17* (22), 33080−33088.

(15) Chouyyok, W.; Warner, C. L.; Mackie, K. E.; Warner, M. G.; Gill, G. A.; Addleman, R. S. Nanostructured Metal Oxide Sorbents for the Collection and Recovery of Uranium from Seawater. *Ind. Eng. Chem. Res.* **2016**, *55* (15), 4195−4207.

(16) Hwang, H.; Kim, M.; Kim, S.; Kim, Y.; Han, M.; Bootharaju, M. S.; Min, M.; Hyeon, T.; Kim, B. H. Ligand-Controlled Fe_3 O_4 Nanoparticles as Reusable Adsorbents for Dye Removal in the Chemical Recycling of Coloured Polyester Textiles. *Nanoscale* **2025**, *17* (48), 28023−28032.

(17) El-sherif, R. M.; Lasheen, T. A.; Jebril, E. A. Fabrication and Characterization of CeO 2 -TiO 2 -Fe 2 O 3 Magnetic Nanoparticles for Rapid Removal of Uranium Ions from Industrial Waste Solutions. *J. Mol. Liq.* **2017**, *241*, 260−269.

(18) Zong, P.; Cao, D.; Cheng, Y.; Zhang, H.; Shao, D.; Wang, S.; He, C.; Zhao, Y. Functionally Reduced Graphene Oxide Supported Iron Oxides Composites as an Adsorbent for the Immobilization of Uranium Ions from Aqueous Solutions. *J. Mol. Liq.* **2017**, *240*, 578−588.

(19) Mahmoud, M. E.; Khalifa, M. A.; Attia, A. A.; Helmy, M. W.; Al-Sherady, M. A. B.; Fekry, N. A. Adsorptive Capture of Uranium (VI) onto a Novel Nanocomposite of Reduced Graphene Oxide@ titanium Dioxide@carboxymethylcellulose. *J. Water Process Eng.* **2023**, *53*, No. 103834.
(20) Fan, F.-L.; Qin, Z.; Bai, J.; Rong, W.-D.; Fan, F.-Y.; Tian, W.; Wu, X.-L.; Wang, Y.; Zhao, L. Rapid Removal of Uranium from Aqueous Solutions Using Magnetic Fe3O4@SiO2 Composite Particles. *J. Environ. Radioact.* **2012**, *106*, 40−46.
(21) Chen, H.; Zhang, Z.; Wang, X.; Chen, J.; Xu, C.; Liu, Y.; Yu, Z.; Wang, X. Fabrication of Magnetic Fe/Zn Layered Double Oxide@ Carbon Nanotube Composites and Their Application for U(VI) and ^{241} Am(III) Removal. *ACS Appl. Nano Mater.* **2018**, *1* (5), 2386−2396.
(22) Nguyen Trung, C.; Begun, G. M.; Palmer, D. A. Aqueous Uranium Complexes. 2. Raman Spectroscopic Study of the Complex Formation of the Dioxouranium(VI) Ion with a Variety of Inorganic and Organic Ligands. *Inorg. Chem.* **1992**, *31* (25), 5280−5287.
(23) Bernhard, G.; Geipel, G.; Brendler, V.; Nitsche, H. Uranium Speciation in Waters of Different Uranium Mining Areas. *J. Alloys Compd.* **1998**, *271*−*273*, 201−205.
(24) Priyadarshini, N.; Sampath, M.; Kumar, S.; Mudali, U. K.; Natarajan, R. A Combined Spectroscopic and Light Scattering Study of Hydrolysis of Uranium(VI) Leading to Colloid Formation in Aqueous Solutions. *J. Radioanal. Nucl. Chem.* **2013**, *298* (3), 1923−1931.
(25) Kanematsu, M.; Perdrial, N.; Um, W.; Chorover, J.; O'Day, P. A. Influence of Phosphate and Silica on U(VI) Precipitation from Acidic and Neutralized Wastewaters. *Environ. Sci. Technol.* **2014**, *48* (11), 6097−6106.
(26) Müller, K.; Brendler, V.; Foerstendorf, H. Aqueous Uranium-(VI) Hydrolysis Species Characterized by Attenuated Total Reflection Fourier-Transform Infrared Spectroscopy. *Inorg. Chem.* **2008**, *47* (21), 10127−10134.
(27) Krestou, A.; Panias, D. Uranium(VI) Speciation Diagrams in the $UO^{22+}/CO^{32-}/H_2O$ System at 25 °C, 2004.
(28) Liu, Z.; Liang, Y.; Zhu, P.; Xu, S.; Fei, J.; Uralbekov, B.; Wang, Y. Uranium Contamination in Groundwater: Sources, Speciation, Transformations, Migration, and Remediation Strategies. *ACS EST Water* **2025**, *5*, 4301.
(29) Kumar, A.; Agarwal, R.; Kumar, K.; Kumar, G.; Kumar, S.; Sharma, M.; Pandey, T.; Ali, M.; Srivastava, A.; Kumar, R.; Kumar, D.; Gajbhiye, R. L.; Murti, K.; Dhingra, S.; Pothuraju, N.; Peraman, R.; Bishwapriya, A.; Sharma, A.; Khandelwal, C.; Singh, M.; Ghosh, A. K. Discovery of Uranium Content in Breastmilk and Assessment of Associated Health Risks for Mothers and Infants in Bihar, India. *Sci. Rep.* **2025**, *15* (1), No. 41389.
(30) Liu, J.; Fan, X.; Ni, J.; Cai, M.; Cai, D.; Jiang, Y.; Mo, A.; Miran, W.; Peng, T.; Long, X.; Yang, F. Mitigation of Uranium Toxicity in Rice by Sphingopyxis Sp. YF1: Evidence from Growth, Ultrastructure, Subcellular Distribution, and Physiological Characteristics. *Plant Physiol. Biochem.* **2024**, *214*, No. 108958.
(31) Bhandari, D.; Wells, S. M.; Retterer, S. T.; Sepaniak, M. J. Characterization and Detection of Uranyl Ion Sorption on Silver Surfaces Using Surface Enhanced Raman Spectroscopy. *Anal. Chem.* **2009**, *81* (19), 8061−8067.
(32) Lu, G.; Haes, A. J.; Forbes, T. Z. Detection and Identification of Solids, Surfaces, and Solutions of Uranium Using Vibrational Spectroscopy. *Coord. Chem. Rev.* **2018**, *374*, 314−344.
(33) Lu, G.; Forbes, T. Z.; Haes, A. J. Evaluating Best Practices in Raman Spectral Analysis for Uranium Speciation and Relative Abundance in Aqueous Solutions. *Anal. Chem.* **2016**, *88* (1), 773−780.
(34) Liger, E.; Charlet, L.; Van Cappellen, P. Surface Catalysis of Uranium(VI) Reduction by Iron(II). *Geochim. Cosmochim. Acta* **1999**, *63* (19−20), 2939−2955.
(35) Nayak, T.; Mukherjee, S.; Kini, A. R.; Islam, M. R.; Nagar, A.; Seth, S.; Pradeep, T. Cellulose-Derived Nanomaterials for Affordable and Rapid Remediation of Uranium in Water. *ACS Sustainable Chem. Eng.* **2025**, *13* (4), 1838−1850.
(36) Cai, Y.; Chen, L.; Yang, S.; Xu, L.; Qin, H.; Liu, Z.; Chen, L.; Wang, X.; Wang, S. Rational Synthesis of Novel Phosphorylated Chitosan-Carboxymethyl Cellulose Composite for Highly Effective Decontamination of U(VI). *ACS Sustainable Chem. Eng.* **2019**, *7* (5), 5393−5403.
(37) Wang, C.-Z.; Lan, J.-H.; Wu, Q.-Y.; Luo, Q.; Zhao, Y.-L.; Wang, X.-K.; Chai, Z.-F.; Shi, W.-Q. Theoretical Insights on the Interaction of Uranium with Amidoxime and Carboxyl Groups. *Inorg. Chem.* **2014**, *53* (18), 9466−9476.
(38) Fairley, N.; Fernandez, V.; Richard-Plouet, M.; Guillot-Deudon, C.; Walton, J.; Smith, E.; Flahaut, D.; Greiner, M.; Biesinger, M.; Tougaard, S.; Morgan, D.; Baltrusaitis, J. Systematic and Collaborative Approach to Problem Solving Using X-Ray Photoelectron Spectroscopy. *Appl. Surf. Sci. Adv.* **2021**, *5*, No. 100112.
(39) Ho, Y. Review of Second-Order Models for Adsorption Systems. *J. Hazard. Mater.* **2006**, *136* (3), 681−689.
(40) Eyley, S.; Thielemans, W. Surface Modification of Cellulose Nanocrystals. *Nanoscale* **2014**, *6* (14), 7764−7779.
(41) Blilid, S.; Katir, N.; El Kadib, A.; Lahcini, M.; Flaud, V.; Alonso, B.; Belamie, E. Phosphorylated Chitin and Cellulose Nanocrystals as Colloidal Bio-Templates towards Mesoporous Aluminophosphates. *New J. Chem.* **2025**, *49* (15), 6469−6483.
(42) Mukherjee, S.; Kumar, A. A.; Sudhakar, C.; Kumar, R.; Ahuja, T.; Mondal, B.; Srikrishnarka, P.; Philip, L.; Pradeep, T. Sustainable and Affordable Composites Built Using Microstructures Performing Better than Nanostructures for Arsenic Removal. *ACS Sustainable Chem. Eng.* **2019**, *7* (3), 3222−3233.
(43) Hsi, C.-k. D.; Langmuir, D. Adsorption of Uranyl onto Ferric Oxyhydroxides: Application of the Surface Complexation Site-Binding Model. *Geochim. Cosmochim. Acta* **1985**, *49* (9), 1931−1941.
(44) Hiemstra, T.; Riemsdijk, W. H. V.; Rossberg, A.; Ulrich, K.-U. A Surface Structural Model for Ferrihydrite II: Adsorption of Uranyl and Carbonate. *Geochim. Cosmochim. Acta* **2009**, *73* (15), 4437−4451.
(45) Wazne, M.; Korfiatis, G. P.; Meng, X. Carbonate Effects on Hexavalent Uranium Adsorption by Iron Oxyhydroxide. *Environ. Sci. Technol.* **2003**, *37* (16), 3619−3624.
(46) Zhang, W.-J.; Huo, C.-F.; Feng, G.; Li, Y.-W.; Wang, J.; Jiao, H. Dehydration of Goethite to Hematite from Molecular Dynamics Simulation. *THEOCHEM* **2010**, *950* (1−3), 20−26.
(47) Liu, H.; Guo, H.; Li, P.; Wei, Y. Transformation from δ-FeOOH to Hematite in the Presence of Trace Fe(II). *J. Phys. Chem. Solids* **2009**, *70* (1), 186−191.
(48) Snow, C. L.; Lee, C. R.; Shi, Q.; Boerio-Goates, J.; Woodfield, B. F. Size-Dependence of the Heat Capacity and Thermodynamic Properties of Hematite (α-Fe2O3). *J. Chem. Thermodyn.* **2010**, *42* (9), 1142−1151.
(49) Sassi, M.; Chaka, A. M.; Rosso, K. M. Ab Initio Thermodynamics Reveals the Nanocomposite Structure of Ferrihydrite. *Commun. Chem.* **2021**, *4* (1), 134.
(50) Song, J.; Niu, X.; Ling, L.; Wang, B. A Density Functional Theory Study on the Interaction Mechanism between H2S and the α-Fe2O3(0001) Surface. *Fuel Process. Technol.* **2013**, *115*, 26−33.
(51) Sandratskii, L. M.; Uhl, M.; Kübler, J. Band Theory for Electronic and Magnetic Properties Of. *J. Phys.: Condens. Matter* **1996**, *8* (8), 983−989.
(52) Martin, G. J.; Cutting, R. S.; Vaughan, D. J.; Warren, M. C. Bulk and Key Surface Structures of Hematite, Magnetite, and Goethite: A Density Functional Theory Study. *Am. Mineral.* **2009**, *94* (10), 1341−1350.
(53) Thevuthasan, S.; Denecke, R. Surface Structure of MBE-Grown a-Fe_2O_3(0001) by Intermediate-Energy X-Ray Photoelectron Diffraction.
(54) Trainor, T. P.; Chaka, A. M.; Eng, P. J.; Newville, M.; Waychunas, G. A.; Catalano, J. G.; Brown, G. E. Structure and Reactivity of the Hydrated Hematite (0001) Surface. *Surf. Sci.* **2004**, *573* (2), 204−224.

https://doi.org/10.1021/acs.langmuir.6c00300
Langmuir 2026, 42, 11219−11228

(55) Wang, X.-G.; Weiss, W.; Shaikhutdinov, S.; Ritter, M.; Petersen, M.; Wagner, F.; Schlögl, R.; Scheffler, M. The Hematite (α- Fe2O3) (0001) Surface: Evidence for Domains of Distinct Chemistry. *Phys. Rev. Lett.* **1998**, *81* (5), 1038−1041.
(56) Tsushima, S.; Rossberg, A.; Ikeda, A.; Müller, K.; Scheinost, A. C. Stoichiometry and Structure of Uranyl(VI) Hydroxo Dimer and Trimer Complexes in Aqueous Solution. *Inorg. Chem.* **2007**, *46* (25), 10819−10826.
(57) Doudou, S.; Arumugam, K.; Vaughan, D. J.; Livens, F. R.; Burton, N. A. Investigation of Ligand Exchange Reactions in Aqueous Uranyl Carbonate Complexes Using Computational Approaches. *Phys. Chem. Chem. Phys.* **2011**, *13* (23), No. 11402.
(58) Grenthe, I.; Fuger, J.; Konings, R. J. M.; Lemire, R. J.; Muller, A. B.; Nguyen-Trung, C.; Wanner, H. Chemical Thermodynamics of Uranium.
(59) Guillaumont, R.; Grenthe, I.et al. Update on the Chemical Thermodynamics of Uranium, Neptunium, Plutonium, Americium and Technetium, 2014.
(60) Clark, D. L.; Conradson, S. D.; Donohoe, R. J.; Keogh, D. W.; Morris, D. E.; Palmer, P. D.; Rogers, R. D.; Tait, C. D. Chemical Speciation of the Uranyl Ion under Highly Alkaline Conditions. Synthesis, Structures, and Oxo Ligand Exchange Dynamics. *Inorg. Chem.* **1999**, *38* (7), 1456−1466.

https://doi.org/10.1021/acs.langmuir.6c00300
Langmuir 2026, 42, 11219−11228